Applied Magnetic Resonance
https://doi.org/10.1007/s00723-022-01470-2

Applied
Magnetic Resonance

ORIGINAL PAPER

Gradient Coil Design and Optimization for an Ultra-Low-Field MRI System

Sheng Shen[1] · Neha Koonjoo[2] · Xiaohan Kong[1] · Matthew S. Rosen[2,3,4] · Zheng Xu[1]

Received: 5 January 2022 / Revised: 14 March 2022 / Accepted: 17 March 2022

Abstract

Gradient coils are used to generate the spatially varying gradient magnetic fields used to phase- and frequency-modulate the nuclear magnetic resonance (NMR) signal and enable position encoding in magnetic resonance imaging (MRI). The continuous-current–density-based method of gradient coil design has been well developed in mathematical modeling, however, practical design as it relates to the experimental realization of simulated gradient coil designs and their ultimate performance has not been well studied. In this work, we design and build a planar gradient coil system, consisting of X, Y, and Z gradient coils, for use in a 6.5 mT ultra-low-field MRI (ULF MRI) system. Specifically, we designed each gradient coil using the equivalent magnetic dipole method (EMDM), and further studied its realization by analyzing gradient-coil geometric parameters, including size, gap, conductor pattern, and conductor density. The geometric parameters are varied during the design of an optimal gradient coil and then analyzed using finite-element-method (FEM) simulations to reveal the relationship between the geometric parameters and gradient coil performance. Based on EMDM and the geometric parameter analysis, we arrive at an optimal gradient coil system whose performance was evaluated by FEM simulation and magnetic field measurement.

1 Introduction

MRI technology has demonstrated its essential role in medical imaging, clinical diagnosis, and scientific research. MRI at very-low (VLF, < 100 mT) and ultra-low (ULF, < 10 mT) magnetic field is an encouraging paradigm to enable lower cost and mobile scanners [1–5]. However, these low-field opportunities have been neglected

Matthew S. Rosen and Zheng Xu contributed equally to this work.

✉ Zheng Xu
xuzheng@cqu.edu.cn

Extended author information available on the last page of the article

Published online: 28 April 2022

for many years generally because of low SNR. In recent years, with the development of improved RF electronics, computational-based MRI pulse sequences [6], and deep-learning-based approaches to image formation [7, 8], the performance of ULF and VLF MRI systems has been significantly improved. In 2015, we described recent developments to our 6.5 mT MRI scanner enabling rapid brain imaging [9]; in 2019, Mäkinen et al. demonstrated ultra-low-field (< 100 μT) MRI using a hybrid MEG-ULF MRI system [10]; in 2020, Cooley et al. demonstrated a prototype of point-of-care MRI scanner based on a Halbach Magnet (80 mT) [11].

In this paper, we focus on gradient coil design and optimization for the 6.5 mT ULF MRI system in our laboratory [9]. Generally, gradient coil design methods can be classified into two types according to the complexity of the winding pattern [12, 13]. The discrete-wire method [14–18] is suitable for the design of gradient coils with simple geometric structures, such as circular, rectilinear, and saddle; well-known gradient coils designed by this method include Maxwell pair and Golay gradient coil. The magnetic-field-source-based method [19–27], also known as the continuous-current–density-based method, is used to design gradient coil by solving the source distribution in the region of gradient coil first; then the source distribution is converted to a conductor pattern. In the magnetic-field-source-based method, the source can be a current density, stream function, or magnetic dipole. Gradient coils designed by the discrete-wire-based method are typically very easy to fabricate, however, gradient performance has much room for improvement. Gradient coils designed by the magnetic-field-source-based method can result in wire patterns that are much more difficult to construct, however, it these designs can result in high gradient performance with current paths that can take full advantage of the available wire area. At present, the state-of-the-art gradient coils in commercial MRI systems are nearly universally designed by the magnetic-field-source-based method.

The magnetic-field-source-based method dates to 1986 when Tuner [19] first proposed the target-field approach to determine a suitable gradient wire pattern. Following this, Tuner further improved this method by including more design requirements in the mathematical modeling [20]. Beside target-field approach, other widely used magnetic-field-source-based methods include harmonic minimization approach [21], stream function method [24], boundary element method (BEM) [25, 28], equivalent magnetic dipole method [26], as well as others [27, 29]. Different methods have their own strengths, and as gradient coil design is a complex, multiparametric process, find utility for specific designs with varying different requirements.

Most of the computational magnetic-field-source-based methods encounter an ill-posed problem in the solving. The ill-posed problem is usually solved by converting it to a regularization problem [30–33], and contemporary research recasts the ill-posed problem as a search for an appropriate regularization term. Power dissipation [22], magnetic energy [29], inductance [20], and a hybrid penalty term [34, 35] have all been examined as regularization terms, again with a specific choice made according to requirements.

We describe here the design of a planar gradient system for an ultra-low-field MRI system where the relationship between the geometric design parameters and gradient coil performance is extensively studied. Specifically, we implemented an approach to gradient coil design using the equivalent magnetic dipole method

(EMDM) to obtain an optimal gradient coil with a high slew rate. The EMDM was previously presented in [26], in this work, we modified the method by exploiting the magnetic field energy as regularization term. With EMDM, we designed several optimized gradient coils with different geometric parameters, and performance was analyzed by FEM simulation of each design. The conclusion obtained from geometric parameter optimization could provide a guide from the perspective of gradient coil fabrication. Finally, an optimal gradient coil system was designed and constructed. The final optimal gradient coil was evaluated by FEM simulation, with a measured nonlinearity of gradient field below 3%, its measured efficiency is greater than 18 μT/(m A).

2 Method

We first introduce the gradient coil performance metric, describe the magnetic field calculation method based on EMDM, and finally describe a mathematical model for gradient coil design.

2.1 Performance Parameters of Gradient Coil System

In the design of an optimized gradient coil system, the evaluation metric needs to be clearly stated. Generally, the performance of gradient coil is parameterized by two things: gradient field nonlinearity and gradient slew rate. Nonlinearity of gradient field is usually defined by (1), where B_c is gradient field generated by gradient coil, and B_i is an ideal gradient field.

$$\delta = \left| \frac{B_G - B_i}{B_i} \right| \times 100\% \tag{1}$$

Nonlinearity is related to distortion of MRI images: the greater the nonlinearity, the worse the distortion. At present, a maximum nonlinearity of 5% is broadly accepted as a typical value. The slew rate of gradient field is related to scanning time of MRI: the higher the slew rate, the faster the ability to traverse *k*-space. It is also worth noting that peripheral nerve stimulation (PNS) ultimately limits the maximum slew rate of a gradient coil for human use, therefore the maximum achievable slew rate should be determined with concerning the maximum gradient field and specific imaging trajectory. The slew rate of the gradient field is proportional to the time-rate of change of the current in the gradient coil. The current, i, in a gradient coil is

$$L\frac{\mathrm{d}i}{\mathrm{d}t} + Ri = V_a, \tag{2}$$

where V_a denotes the voltage supplied by the gradient amplifier, L and R denote the inductance and resistance of the gradient coil. When R is relatively small, the slew rate of the current S_i is

$$S_{\mathrm{i}} \approx \frac{\mathrm{d}i}{\mathrm{d}t} = \frac{V_{\mathrm{a}}}{L}. \tag{3}$$

The gradient coil efficiency, η, is defined as gradient magnetic field generated per unit current, which may be expressed

$$\eta = \frac{G}{i}, \tag{4}$$

where G denotes gradient field strength in the ROI. From (3) and (4), the slew rate of gradient field, S_G, can be written

$$\mathrm{S_G}=\frac{\mathrm{d}G}{\mathrm{d}t} = \eta \cdot \frac{\mathrm{d}i}{\mathrm{d}t} \approx \frac{\eta}{L} \cdot V_{\mathrm{a}}. \tag{5}$$

In what follows, when evaluating gradient field slew rate, the excitation voltage V_{a} is normalized to 1, then, so S_{G} simplifies to η/L.

2.2 Magnetic Field Calculation Based on the Equivalent Magnetic Dipole Method

The gradient system described in this paper interfaces with our ultra-low-field planar electromagnet MRI system. To match the geometry of the electromagnet, the geometry of each gradient coil is also planar as shown in Fig. 1.

The equivalent magnetic dipole method (EMDM), previously presented in our work [26] is used to design the gradient coils; in this paper, we modified the EMDM by introducing the magnetic energy as a regularization term instead of dissipating energy applied in [26]. To build the mathematical model of EMDM, we first partition the planar winding area of the gradient coil into small, identical rectangles, each consisting of a rectangle-shaped current loop as shown as Fig. 2. The rectangle-shaped current loop is the equivalent magnetic dipole; the limit of a closed loop of electric current as the linear size of the source is reduced to zero while keeping the

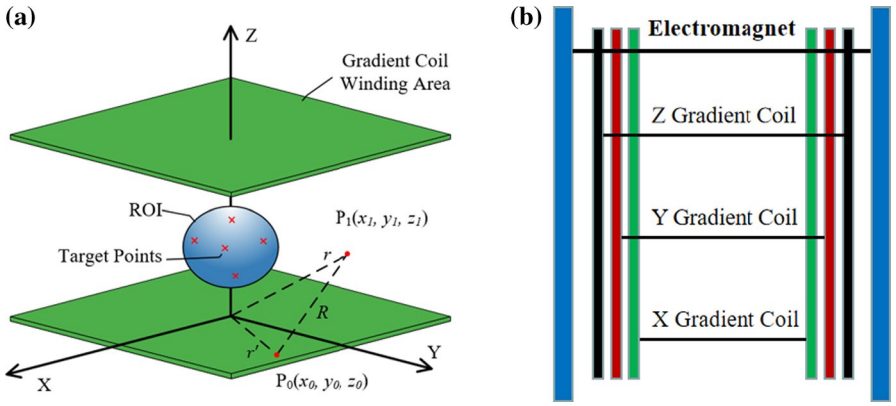

Fig. 1 **a** Planar gradient coil, **b** planar gradient coil system located within the planar electromagnet ULF MRI scanner

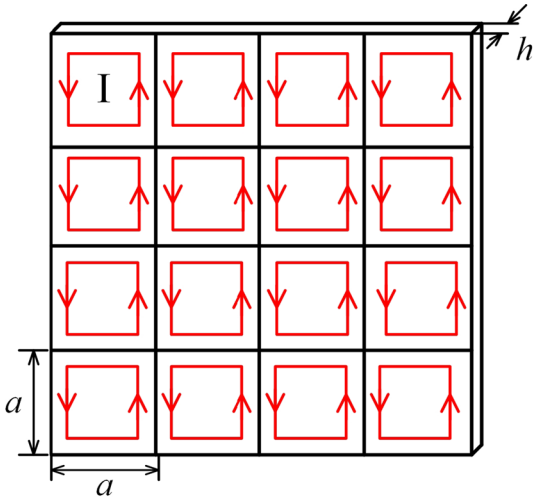

Fig. 2 Diagram of partitioned winding area tiled with rectangle-shaped current loops

magnetic moment constant is a magnetic dipole (Fig. 3). The magnetic moment $\boldsymbol{m}$ of a magnetic dipole is calculated from (6).

$$\boldsymbol{m} = IS \cdot \boldsymbol{n}. \tag{6}$$

where $\boldsymbol{n}$ is the normal vector, I and S are the current and area of the magnetic moment, respectively. Thus in this work, the magnetic dipole moment $\boldsymbol{m}_\mathbf{e}$ of equivalent magnetic dipole is calculated according to formula (6) as (7).

$$\boldsymbol{m}_\mathbf{e} = I_\mathrm{e} a^2 \cdot \boldsymbol{n}_\mathbf{e}, \tag{7}$$

where, $\boldsymbol{n}_\mathbf{e}$ is the normal vector, I_e and a are the current and side length of the current loop in Fig. 2, respectively. The side length of the equivalent magnetic dipole determines its spatial resolution for a fixed gradient coil winding area. Reducing the side

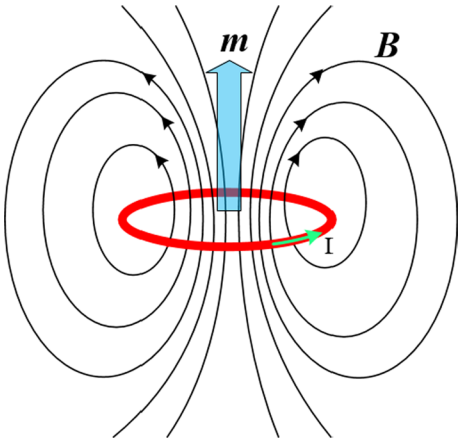

Fig. 3 Diagram of a magnetic dipole

length can enhance the spatial resolution which in turn improves the smoothness of the pattern of gradient coil. However it also dramatically increases computational cost for the gradient coil optimization problem. A good balance between equivalent magnetic dipole spatial resolution and computational cost was found when the side length of equivalent magnetic dipole was set to 1/40 of the side length of the planar winding area.

The magnetic field $\boldsymbol{B}$ generated by a magnetic dipole $\boldsymbol{m}$, is usually calculated as

$$\boldsymbol{B} = \frac{\mu_0}{4\pi}(\boldsymbol{m}\cdot\nabla)\nabla\frac{1}{R} = \frac{\mu_0}{4\pi}\nabla\left(\boldsymbol{m}\cdot\nabla\frac{1}{R}\right) = -\frac{\mu_0}{4\pi}\nabla\left(\boldsymbol{m}\cdot\frac{(\boldsymbol{r}-\boldsymbol{r'})}{|R|^3}\right), \tag{8}$$

where R is the distance between magnetic field and any point in space, $\boldsymbol{r}$ is a vector used to describe the position of any point in space, $\boldsymbol{r'}$ is a vector to describe the position of equivalent magnetic dipole. The magnetic field $\boldsymbol{B}_\mathbf{e}$ generated by an equivalent magnetic dipole is calculated from (8),

$$\boldsymbol{B}_\mathbf{e} = -\frac{\mu_0 I_\mathrm{e} a^2}{4\pi}\nabla\left(\frac{\boldsymbol{n}_\mathbf{e}\cdot(\boldsymbol{r}-\boldsymbol{r'})}{|R|^3}\right). \tag{9}$$

From (9), we can calculate the magnetic field in the region of interest (ROI) generated by the equivalent magnetic dipole matrix from Fig. 2. Theoretically, the gradient field in ROI can be obtained by adjusting the current value of each equivalent magnetic dipole, so the gradient field $\boldsymbol{B}_\mathbf{G}$ can be determined by a specific current loop matrix $\boldsymbol{I}_\mathbf{G}$, Their relationship then could be described by a function f,

$$\boldsymbol{B}_\mathbf{G} = f(\boldsymbol{I}_\mathbf{G}) \tag{10}$$

2.3 Magnetic Dipole Optimization Based on Tikhonov Regularization

Formula (10) can be used to calculate the magnetic field in the ROI generated by a given current loop matrix. It cannot however be used to determine a unique current loop matrix for a given magnetic field; solving the current loop matrix for a given gradient field is an ill-posed inverse problem with a non-unique and unstable solution. This means that a given gradient field can be generated by different current loop configurations, and a slight change in current loop matrix might result in dramatic changes to the gradient field.

Generally, ill-posed inverse problems are solved using the Tikhonov regularization approach, which recasts the problem as a minimization problem with a penalty term, i.e.:

$$\mathbf{Min}:\ F = (f(\boldsymbol{I}_\mathbf{G}) - \boldsymbol{B}_\mathrm{i})^2 + \lambda G(\boldsymbol{I}_\mathbf{G}). \tag{11}$$

The penalty term, also known as the regularization term, is used to track instability; a feasible solution is one that yields a low value of $G(\boldsymbol{I}_\mathbf{G})$.

In this work, we chose the magnetic energy, W_B of the equivalent magnetic dipole as the regularization term, which is calculated

$$W_{\mathrm{B}} = \frac{1}{2}\int \boldsymbol{A}\cdot\boldsymbol{J}\mathrm{d}V, \tag{12}$$

where $\boldsymbol{A}$ denotes vector magnetic potential of equivalent magnetic dipole, calculated from

$$\boldsymbol{A} = \frac{\mu_0}{4\pi R^2}(\boldsymbol{m}_{\mathbf{e}} \times (\boldsymbol{r} - \boldsymbol{r'})). \tag{13}$$

$\boldsymbol{J}$ is the equivalent current density, the components of which are calculated with (14), with m is the index enumerating magnetic dipoles, n is the index of equivalent magnetic dipole in a row, the diagram of current density calculation is shown as Fig. 4.

$$\begin{aligned} \boldsymbol{J}_{\boldsymbol{m},\boldsymbol{i}} &= (I_{m+1} - I_m)/a \\ \boldsymbol{J}_{\boldsymbol{m},\boldsymbol{j}} &= (I_{m+n} - I_m)/a \end{aligned} \tag{14}$$

The magnetic energy of a gradient coil can also be calculated from

$$W_{\mathrm{B}} = \frac{1}{2}LI_0^2. \tag{15}$$

Using magnetic energy as a regularization term, we can obtain a gradient coil with low inductance. This follows from (5), whereby the lower the inductance, the higher the attainable slew rate. Thus, these two essential performance parameters of gradient design, field nonlinearity, and slew rate are all considered in this formulation of the minimization problem, $\boldsymbol{F}$.

2.4 Stream Function

The matrix of optimal current loops, $\boldsymbol{I}$, can be obtained by solving the minimization problem of (11). This current loop matrix is the stream function of an equivalent

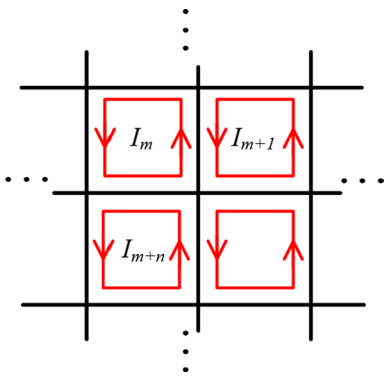

Fig. 4 Diagram of current density calculation

magnetic current density, $\boldsymbol{J}_{\mathbf{e}}$. According to the stream function method [24], the contours of the current loop matrix become the winding pattern for the gradient coil.

The current density satisfies the continuity equation,

$$\nabla \cdot \boldsymbol{J} = 0, \tag{16}$$

therefore we could use a hypothetical scalar function, S_0, and a unit-length vector $\boldsymbol{n_0}$ to represent current density as

$$\boldsymbol{J} = \nabla \times (S_0 \cdot \boldsymbol{n_0}). \tag{17}$$

The magnetization of an equivalent magnetic dipole, $\boldsymbol{M}$, is calculated by (18).

$$\boldsymbol{M} = \frac{\sum \boldsymbol{m}}{V} = \frac{\boldsymbol{m}_{\mathbf{e}}}{V} = \frac{I \cdot a^2}{a^2 \cdot h} \cdot \boldsymbol{n} = \frac{I}{h} \cdot \boldsymbol{n}, \tag{18}$$

where V denotes the volume occupied by magnetic dipoles, h denotes the thickness of the volume, shown in Fig. 2. The vector magnetic potential of magnetization $\boldsymbol{M}$, is calculated from

$$\boldsymbol{A}_{\mathbf{m}} = \frac{\mu_0}{4\pi}\left(\int_V \frac{1}{R} \nabla \times \boldsymbol{M}(\boldsymbol{r'}) \mathrm{d}V + \int_{S_s} \frac{\boldsymbol{M}(\boldsymbol{r'}) \times \boldsymbol{n}_{0,s}}{R} \mathrm{d}S_s \right), \tag{19}$$

where $\boldsymbol{n}_{0,s}$ denotes the unit-length vector of the surface of equivalent magnetic dipoles.

The vector magnetic potential of a current density $\boldsymbol{J}$ is calculated from

$$\boldsymbol{A}_{\mathbf{J}} = \frac{\mu_0}{4\pi} \int_V \frac{1}{R} \nabla \times \boldsymbol{J} \mathrm{d}V. \tag{20}$$

According to (19) and (20), the relationship between the magnetic-dipole magnetization and its equivalent magnetic current density $\boldsymbol{J}_{\mathbf{e}}$ could be expressed as (21).

$$\boldsymbol{J}_{\mathbf{e}} = \nabla \times \boldsymbol{M} \tag{21}$$

Combining (18) and (21), one gets

$$\boldsymbol{J}_{\mathbf{e}} = \nabla \times \left(\frac{I}{h} \cdot \boldsymbol{n} \right). \tag{22}$$

Since h is a constant, from (22) the current loop value, I is the stream function of the equivalent magnetic current density, $\boldsymbol{J}_{\mathbf{e}}$. Thus, the contours of the current loop matrix are the winding pattern of the gradient coil.

3 Geometric Parameter Analysis

The geometric parameters of a gradient coil include wire winding density, regularization coefficient, gradient coil gap, and gradient coil size. As described above, the optimal solution of the minimization problem, $\boldsymbol{F}$, leads to the steam function, and the contours of the stream function themselves are the gradient coil winding pattern. For a specific stream function, we can plot it using contour maps with different number of contours; in this way, the wire density becomes the contour density. The regularization coefficient determines the complexity of gradient coil pattern as it pertains to the performance of the gradient coil. The gap simply denotes the distance between two plates of the planar gradient coil. Gradient coil size was parameterized by the side length of the planar coil winding area.

To reveal the relationship between geometric parameters of gradient coil and its performance, we implemented a gradient coil design workflow using EMDM. Specifically, we adjusted the geometric parameters and designed a gradient coil whose gradient-field direction is perpendicular to that of scanner static magnetic field. And then analyzed this gradient coil using FEM simulation. Before implementing the computational parameter analysis, we manually explored a range of parameters to obtain a reasonable starting location. All the EDMD design optimizations start from this location where the regularization coefficient is 10^{-20}; the gradient coil gap is 0.8 m, the side length of planar winding area is 1 m and the number of contours is 12. In the following sections, the influence of changing each of these parameters is discussed.

3.1 Gradient Coil Density

In gradient coil density analysis, we obtain an optimal stream function distribution and plot it using five contour maps with different number of contours. Specifically, in stream function solving, the regularization coefficient was set to 10^{-20}, the gradient coil gap was set to 0.8 m, the side length of planar winding area was set to 1 m and the number of contours was set to 8, 10, 12, 14, and 16. Figure 5 shows the optimal stream function and its corresponding gradient pattern in different coil density. Table 1 shows the FEM simulation result with an ROI given by a spherical region with radius of 150 mm, target points uniformly distributed on the surface of the ROI, and the nonlinearity of gradient field is the average value of relative error between the simulated magnetic field and the ideal gradient field at target fields; Fig. 6 shows the relationship between the gradient coil density and its performance.

According to the results shown in Fig. 5, the average nonlinearity of gradient field first decreases and then increases with increasing coil density. However, the difference between the maximum and minimum nonlinearity is less than 0.4%, so gradient coil density has no practical effect on the nonlinearity of gradient field. The inductance and gradient coil efficiency increases, while the slew rate decreases with increasing coil density, so adjusting gradient coil density, leads to

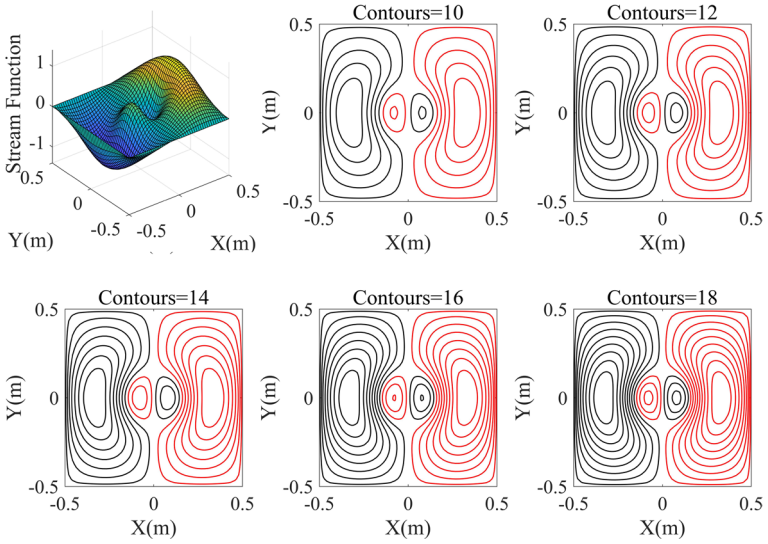

Fig. 5 Optimal stream function and corresponding gradient coil pattern in different coil density, (Regularization coefficient = 10^{-20}, gap = 0.8 m, side length = 1 m, the number of contours = 10, 12, 14, 16, 18)

Table 1 Performance parameters (gradient coil density)

Number of contours	10	12	14	16	18
Average nonlinearity (%)	0.9346	0.7726	0.6271	0.6827	0.8418
efficiency (μT/(m· A))	12.4461	14.7266	16.9946	19.3358	21.5478
Inductance (μH)	77.8880	103.9577	133.7824	167.1161	205.5738
Slew rate (T/(m· A· H))	0.1598	0.1417	0.1270	0.1157	0.1048

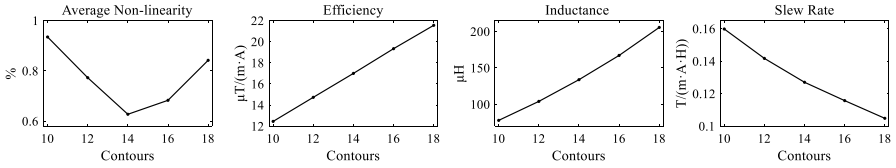

Fig. 6 The relationship between gradient coil density and its performance parameters, (Regularization coefficient = 10^{-20}, gradient coil gap = 0.8 m, side length = 1 m, the number of contours = 10, 12, 14, 16, 18)

a corresponding increase in either efficiency or slew rate, with a decrease in the corresponding other parameters. Thus, gradient coil density adjustment can be used to tune the gradient coil efficiency, and considering that both the efficiency and slew rate are very important parameters in gradient coil design, the gradient coil density should be as low as possible with the premise of meeting the efficiency requirements.

3.2 Regularization Coefficient

In an analysis of the regularization coefficient, we generated five optimized gradient coils. Specifically, in the stream function solving, the gradient coil gap was set to 0.8 m, the side length of the planar winding area was set to 1 m and the regularization coefficients were set to 10^{-22}, 10^{-21}, 10^{-20}, 10^{-19}, and 10^{-18}; the number of contours was set to 12. Figure 7 shows the optimal stream function and its corresponding gradient pattern; Table 2 shows the FEM simulation results; Fig. 8 shows the relationship between the regularization coefficient and its performance.

The optimized gradient coil patterns were obtained by adjusting the regularization coefficient. According to the FEM simulation results in Fig. 8, the nonlinearity of gradient field, the gradient coil efficiency and gradient coil slew rate all increase with increasing regularization coefficient, and only the inductance decrease.

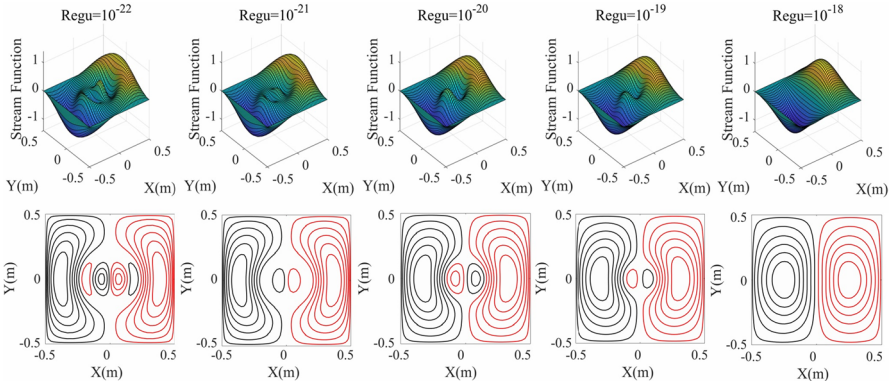

Fig. 7 Optimal stream function and corresponding gradient coil pattern obtained with adjusting the regularization coefficients. (Regularization coefficient = 10^{-22}, 10^{-21}, 10^{-20}, 10^{-19}, 10^{-18}, gap = 0.8 m, side length = 1 m, the number of contours = 12)

Table 2 Performance parameters (regularization coefficient)

Regularization coefficient	10^{-22}	10^{-21}	10^{-20}	10^{-19}	10^{-18}
Average nonlinearity (%)	0.1411	1.3785	0.7446	2.709	6.1784
Efficiency (μT/(m· A))	10.7060	11.8082	14.7226	17.1268	21.6507
Inductance (μH)	112.6150	103.9928	103.9577	98.3855	92.0000
Slew rate (T/(m· A· H))	0.0951	0.1135	0.1416	0.1741	0.2353

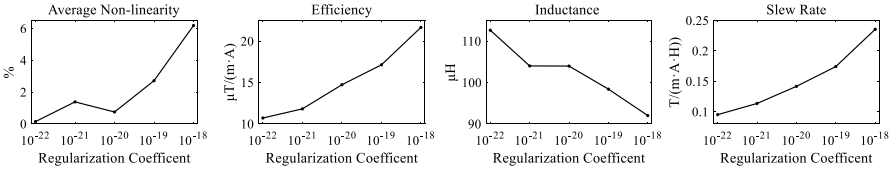

Fig. 8 Relationship between regularization coefficient and its performance parameters, (Regularization coefficient = 10^{-22}, 10^{-21}, 10^{-20}, 10^{-19}, 10^{-18}, gap = 0.8 m, side length = 1 m, the number of contours = 12)

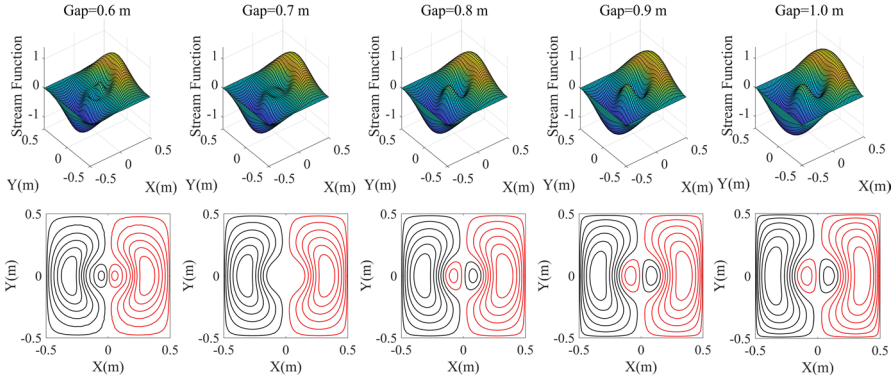

Fig. 9 Optimal stream function and corresponding gradient coil pattern obtained with adjusting the gradient coil gap, (Regularization coefficient = 10^{-20}, gap = 0.6, 0.7, 0.8, 0.9, 1.0 m, side length = 1 m, the number of contours = 12)

Table 3 Performance parameters (Gradient coil gap)

Gap (m)	0.6	0.7	0.8	0.9	1.0
Average nonlinearity (%)	6.97	0.63	0.74	1.03	3.75
Efficiency (μT/(m· A))	21.46	19.14	14.72	11.24	9.95
Inductance (μH)	92.02	95.07	103.96	112.18	118.09
Slew rate (T/(m· A· H))	0.23	0.20	0.14	0.10	0.08

Remarkably, increasing regularization coefficient changes the gradient coil inductance, efficiency and slew rate change with a positive trend, while gradient filed linearity changes with a negative trend. The regularization coefficient has a significant effect on the nonlinearity, so adjusting the regularization term can effectively adjust the linearity of gradient field. In regularization coefficient adjustment, the linearity and slew rate of gradient field vary with opposite signs; it is necessary to balance between these performance parameters in gradient coil design. Moreover, the complexity of gradient pattern is hard to quantify, but it is also related to the regularization coefficient, shown as Fig. 7, and should be considered in gradient coil design.

3.3 Gradient Coil Gap

In gradient coil gap analysis, we generated five optimized gradient coils using EMDM. Specifically, in the stream function solving, the regularization coefficients were set to 10^{-20}, the side length of planar winding area was set to 1 m and the gradient coil gap was set to 0.6, 0.7, 0.8, 0.9 and 1.0 m; the number of contours was set to 12. Figure 9 shows the optimal stream function and its corresponding gradient pattern; Table 3 shows the FEM simulation results; Fig. 10 shows the relationship between gradient coil gap and its performance.

The optimized gradient coil patterns were obtained by adjusting gradient coil gap. According to the FEM simulation results in Fig. 10, the nonlinearity

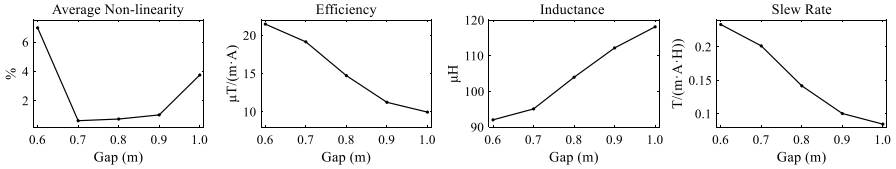

Fig. 10 Relationship between gradient coil gap and its performance parameters (Regularization coefficient = 10^{-20}, gap = 0.6, 0.7, 0.8, 0.9, 1.0 m, side length = 1 m, the number of contours = 12)

of gradient field first decreases and then increases with increasing gradient coil gap. The maximum nonlinearity value is close to 7% and the minimum value is less than 1%, a significant difference. Both the efficiency and slew rate of gradient coil decrease, while the inductance increases with increasing gradient coil gap. According to the trend of nonlinearity, there exists an optimal gradient coil gap once the other geometric parameters are determined. As gradient coil gap increases, all the performance parameters, except for nonlinearity of gradient field, change with a negative trend. Thus, in gradient coil design, the gradient coil gap should be as large as possible with the goal of meeting the requirement of gradient nonlinearity and maximizing patient space in the MRI scanner.

3.4 Gradient Coil Size

In gradient coil size analysis, we generated five optimized gradient coils using EMDM. Specifically, in the stream function solving, the regularization coefficients were set to 10^{-20}, the gradient coil gap was set to 0.8, the side length of the planar winding area was set to 0.6, 0.8, 1.0, 1.2, and 1.4 m; the number of contours was set to 12. Figure 10 shows the optimal stream function and its corresponding gradient coil pattern; Table 4 shows the FEM simulation results; Fig. 11 shows the relationship between gradient coil size and its performance.

The optimized gradient coil patterns were obtained as a function of gradient coil size. According to the FEM simulation results in Fig. 12, with increasing gradient coil size, the nonlinearity of the gradient field decreases while the other performance parameters increase. As gradient coil size increases, all the performance parameters, except for the inductance of the gradient coil, change with a positive trend. As inductance is a parameter used to evaluate slew rate indirectly, the performance of gradient coil is significantly improved with increased gradient coil size.

Table 4 Performance parameters (Gradient coil size)

Side length (m)	0.6	0.8	1.0	1.2	1.4
Average nonlinearity (%)	2.96	0.96	0.74	0.71	0.43
Efficiency (μT/(m· A))	9.15	12.41	14.72	16.20	17.46
Inductance (μH)	98.00	98.11	103.96	110.59	126.29
Slew rate (T/(m· A· H))	0.09	0.13	0.14	0.15	0.14

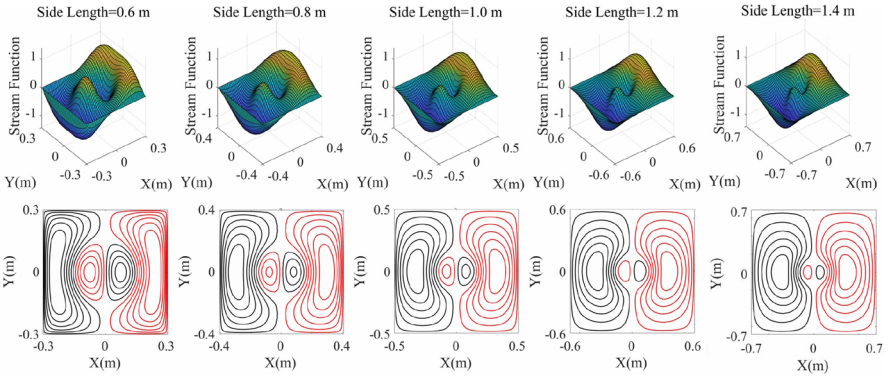

Fig. 11 Optimal stream function and corresponding gradient coil pattern obtained with adjusting the gradient coil size, (Regularization coefficient = 10^{-20}, gap = 0.8 m, side length = 0.6, 0.8, 1.0, 1.2, 1.4 m, the number of contours = 12)

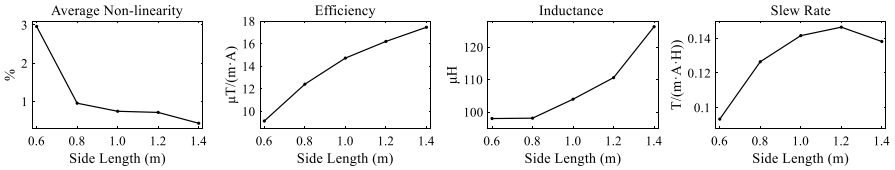

Fig. 12 Relationship between gradient coil size and its performance parameters, (Regularization coefficient = 10^{-20}, gap = 0.8 m, side length = 0.6, 0.8, 1.0, 1.2, 1.4 m, the number of contours = 12)

4 Result

Based on our extensive EMDM simulations and geometric parameter analysis, we designed gradient coils for an ULF MRI system and built a gradient coil prototype. The performance of gradient coil prototype was evaluated by FEM simulation and performance parameter measurement.

4.1 Gradient Coil Design for a ULF MRI System

Our analysis of the impact that geometric parameters have on gradient coil performance provides a basis for parameter tuning in gradient coil design. We adjusted these geometric parameters to design a gradients system that could meet our physical requirements with the best performance. For our scanner, the available area for gradient coil placement is a planar area with a side length of 1.22 m; to allow some space for the gradient coil support structure, a side length for the gradient coil was set to 1.18 m. We pick an imaging ROI located at the isocenter of the magnet having a radius of 150 mm. The maximum distance between the two planes of the ultra-low-field planar electromagnet is around 0.78 m, so all the

Table 5 Design parameters in gradient coil design

	Density	Gap (m)	Regularization coefficient	Side length (m)	Radius of ROI (mm)
X gradient coil	16	0.717	1.2×10^{-21}	1.18	150
Y gradient coil	16	0.743	8×10^{-22}	1.18	150
Z gradient coil	16	0.769	1×10^{-20}	1.18	150

gradient coil gaps are smaller than 0.78 m. A table of the design parameters is given in Table 5.

Figure 13 shows the optimal stream function and gradient coil pattern of X, Y and Z gradient coil. Figure 14 shows field maps on the plane of YOZ, XOZ and XOY, which is generated by X, Y and Z gradient coil, respectively.

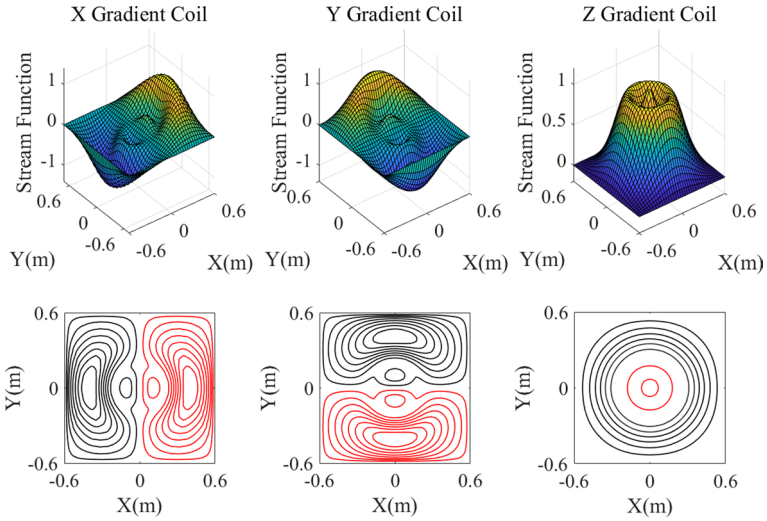

Fig. 13 Design result of gradient coil, **a** X gradient coil, **b** Y gradient coil, **c** Z gradient coil

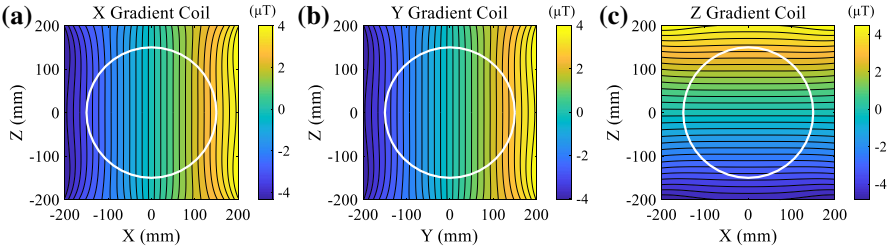

Fig. 14 Simulation result of gradient coil (the radius of white circle is 150 mm), **a** X gradient coil, **b** Y gradient coil, **c** Z gradient coil. The location of filed map and gradient coil are both defined in the coordinate system shown in Fig. 1a

Table 6 Performance parameters of gradient coil

Gradient coil	Maximum nonlinearity (%)	Average nonlinearity (%)	Efficient (μT/(m· A))	Inductance (μH)	Slew rate (T/(m· A· H))	Wire length (m)
X	1.01	0.13	20.89	177.35	0.12	32.03
Y	1.04	0.13	19.39	179.13	0.11	32.41
Z	2.82	0.29	22.54	85.37	0.26	17.15

The performance parameters calculated based on the FEM simulation were shown in Table 6.

4.2 Gradient Coil Prototype

We built a gradient set based on the FEM simulations. Specifically, we cut grooves on acrylic plates using a CNC router with wire paths placed according to the gradient coil pattern shown in Fig. 13. Figure 15 shows the simulated coil traces and the physical gradient coils.

The completed gradient coils are shown in Fig. 16a and the gradient coil system assembled within the electromagnet scanner is shown in (b).

Finally, we measured field maps of different gradient coils, where the gradient coil is powered by a DC power supply (6233A, Agilent) and the magnetic field is measured by a Gaussmeter (8030, F. W. Bell). The field map was shown as Fig. 17a; Fig. 17b shows gradient fields on the midline (along the gradient direction) of each field map. The measured performance parameters are shown in Table 7.

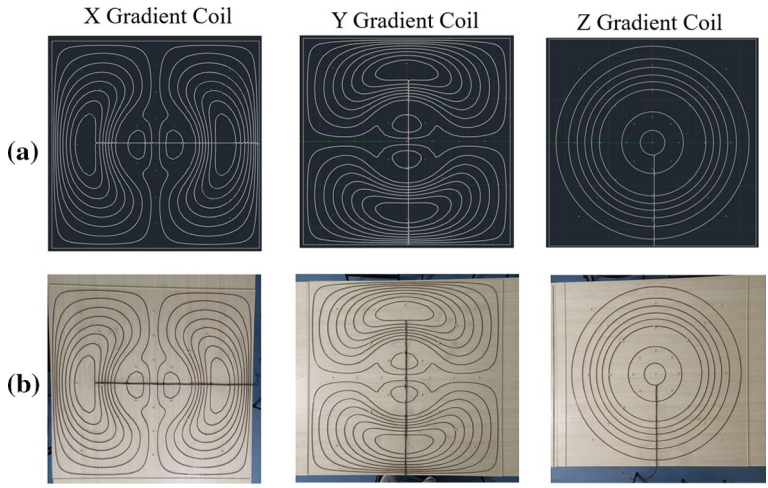

Fig. 15 Gradient coil trace and gradient coil prototype, **a** gradient coil winding trace, **b** gradient coil prototype

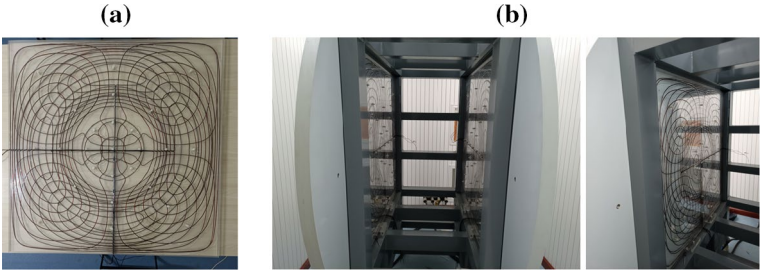

Fig. 16 Gradient coil assembly **a** gradient coil system, **b** assembly picture

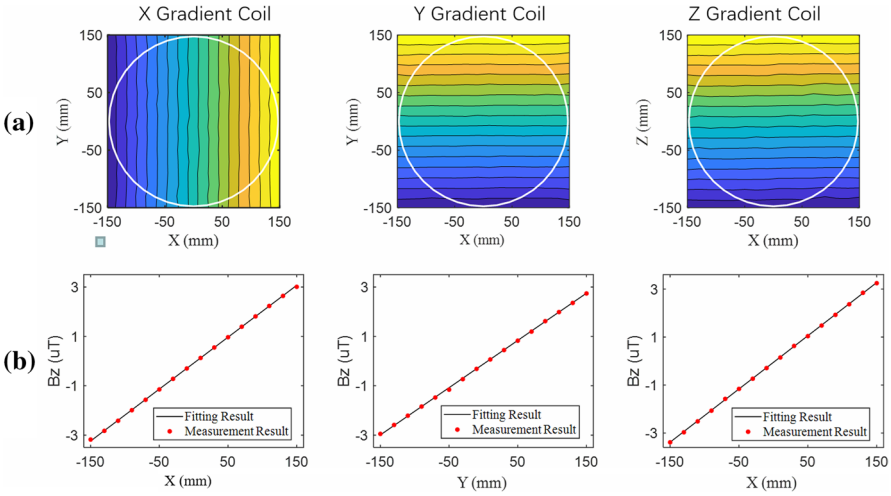

Fig. 17 Measurement result of gradient magnetic field, the location of the filed map and gradient coil are both defined in the coordinate system shown in Fig. 1a

Table 7 Performance parameters of gradient coil

Gradient coil	Maximum non-linearity (%)	Efficient (μT/(m· A))	Inductance (μH)	Resistance (mΩ)	Slew rate (T/(m· A· H))
X	2.02	21.03	188.17	195.69	0.11
Y	1.46	19.15	191.87	198.54	0.10
Z	0.85	22.18	92.24	118.78	0.24

According to the measurements, the nonlinearity of all gradient coil is less than 5%, and the efficiency and slew rate value are consistent with the simulation result.

5 Discussion

It is difficult to optimize the geometric parameters critical to gradient design by explicitly including them into a master mathematical model of gradient coil design. In general, they are usually the initial conditions and preconditions of the mathematical model. In this work, we have studied the qualitative relationship between these physical design parameters and gradient coil performance. The insight obtained from the study of the relationship between these parameters allows one to converge on a family of near-optimal solutions for gradient coil design. We do note that due to the computational complexity involved, the role of each geometric parameter was studied independently, where in fact these geometric parameters may couple to each other. A quantitative and more accurate study of the relationship between the geometric parameters and gradient coil performance still needs further study.

Our analysis of geometric parameters was implemented with the design of a gradient set. Both the X and Y gradient coils, shown in Fig. 13 produce a gradient transverse to the main magnetic field. The conductor pattern of the Z gradient coil, which produces a magnetic field gradient in the same direction of the main magnetic field, is different from that of X and Y gradient coil. We also analyzed the geometric parameters of Z gradient coil using the same approaches described in the *Geometric Parameters Analysis* part of this paper; the conclusion obtained in Z-gradient-coil geometric parameters analysis is consistent with that of the X and Y gradient coils. Notably, we also compared the performance of different gradient coils, and found the efficiency and slew rate of Z gradient coil is significantly better than that of the transverse gradient coils, which is also reflected in the results shown in Tables 6 and 7. Based on this conclusion and that in *Geometric Parameters Analysis* section, we set the gradient coil gap of Z gradient coil to be the largest among X, Y and Z gradient coils.

We also encountered difficulties in the evaluation of gradient field nonlinearity. Theoretically, the gradient field in the center of ROI has the best linearity; however, the nonlinearity is calculated with formula (1), the ideal magnetic field in the center of ROI is close to 0, which means the denominator is close to zero, and that results in high nonlinearity. In the *Geometric Parameters Analysis* section, we use the average relative error at all target points to evaluate the gradient field linearity. As shown in the *Result* section, a field map was obtained for a single plane in the ROI, and we used the maximum relative error at the end of the midline of the plane which is shown as Fig. 17.

6 Summary and Conclusion

In this work, we developed the equivalent magnetic dipole method (EMDM) with the introduction of magnetic energy as a regularization term to condition the ill-posed inverse problem of gradient design. Based on the modified EMDM, we

analyzed the geometric parameters of gradient coil and qualitatively revealed the relationship between these geometric parameters and the gradient coil performance. As a result, we proposed geometric adjustment principles for gradient design and fabrication; geometric-parameter adjustment principles could be used to further optimize the performance of gradient coil designed using magnetic-field-source-based methods. Finally, we designed an optimum gradient coil system and built a prototype.

Acknowledgements We appreciate the help provided by Wei Zhang, Cai Wan, Qing Zhao, and Yuhang Yang in gradient coil winding and assembling. This work was funded by the National Natural Science Foundation of China (52077023), Natural Science Foundation of Chongqing(cstc2020jcyj-msxmX0340), and Shenzhen Science and Technology Innovation Commission (CJGJZD20200617102402006). Data will be made available on reasonable request.

References

1. L.L. Wald, P.C. McDaniel, T. Witzel, J.P. Stockmann, C.Z. Cooley, Low-cost and portable MRI. J. Magn. Reson. Imaging **4**(3), 31 (2019)
2. S. Geethanath, J.T. Vaughan, Accessible magnetic resonance imaging: A review. J. Magn. Reson. Imaging **242**, 190 (2019)
3. J.P. Marques, F.F.J. Simonis, A.G. Webb, Low-field MRI: An MR physics perspective. J. Magn. Reson. Imaging **58**, 1182 (2019)
4. K.N. Sheth et al., Assessment of brain injury using portable, low-field magnetic resonance imaging at the bedside of critically ill patients. JAMA Neurol. **78**(1), 41–47 (2020). https://doi.org/10.1001/jamaneurol.2020.3263
5. M.H. Mazurek et al., Portable, bedside, low-field magnetic resonance imaging for evaluation of intracerebral hemorrhage. Nat. Commun. **12**(1), 5119 (2021). https://doi.org/10.1038/s41467-021-25441-6
6. D. Ma, V. Gulani, N. Seiberlich, K. Liu, J.L. Sunshine, J.L. Duerk, M.A. Griswold, Magnetic resonance fingerprinting. Nature **495**, 187–192 (2013)
7. B. Zhu, J.Z. Liu, S.F. Cauley, B.R. Rosen, M.S. Rosen, Image reconstruction by domain-transform manifold learning. Nature **555**(7697), 487–492 (2018)
8. N. Koonjoo, B. Zhu, G.C. Bagnall, D. Bhutto, M.S. Rosen, Boosting the signal-to-noise of low-field MRI with deep learning image reconstruction. Sci. Rep. **11**(1), 8248 (2021). https://doi.org/10.1038/s41598-021-87482-7
9. M. Sarracanie, C.D. LaPierre, N. Salameh, D.E.J. Waddington, T. Witzel, M.S. Rosen, Low-cost high-performance MRI. Sci. Rep. **5**(1), 15177 (2015)
10. A.J. Mäkinen, K.C.J. Zevenhoven, R.J. Ilmoniemi, Automatic spatial calibration of ultra-low-field MRI for high-accuracy hybrid MEG–MRI. IEEE Trans. Med. Imaging **38**(6), 1317–1327 (2019)
11. C.Z. Cooley, P.C. McDaniel, J.P. Stockmann et al., A portable scanner for magnetic resonance imaging of the brain. Nat. Biomed. Eng. **5**, 229–239 (2021)
12. R. Turner, Gradient coil design: A review of methods. Magn. Reson. Imaging **11**(7), 903–920 (1993)
13. S.S. Hidalgo-Tobon, Theory of gradient coil design methods for magnetic resonance imaging. Concepts Magn. Reason. Part A **36A**(4), 223–242 (2010)
14. F. Roméo, D.I. Hoult, Magnet field profiling: Analysis and correcting coil design. Magn. Reason. Med. **1**, 44–65 (1984)
15. Golay MJE. Magnetic Field Control Apparatus. US Patent 3,515,979 (1957).
16. E.M. Purcell, Helmholtz coils revisited. Am. J. Phys. **57**, 18–22 (1989)
17. T.A. Frenkiel, A. Jasinski, P.G. Morris, Apparatus for generation of magnetic field gradient waveforms for NMR imaging. J. Phys. E Sci. Instrum. **21**, 374–377 (1988)
18. B.H. Suits, D.E. Wilken, Improving magnetic field gradient coils for NMR imaging. J. Phys. E Sci. Instrum. **22**, 565–573 (1989)

19. R. Turner, A target field approach to optimal coil design. J. Phys. D-Appl. Phys. **19**(8), L147–L151 (1986)
20. R. Turner, Minimum inductance coils. J. Phys. E-Sci. Instrum. **21**(10), 948–952 (1988)
21. J.W. Carlson, K.A. Derby, K.C. Hawryszko, M. Weideman, Design and evaluation of shielded gradient coils. Magn. Reason. Med. **26**, 191–206 (1992)
22. S. Pissanetzky, Minimum energy MRI gradient coils of general geometry. Meas. Sci. Technol. **3**(7), 667 (1992)
23. M. Poole, R. Bowtell, Novel gradient coils designed using a boundary element method. Concepts Magn. Reason. Part B Magn. Reason. Eng. **31B**(3), 162–175 (2007)
24. D. Tomasi, Stream function optimization for gradient coil design. Magn. Reson. Med. **45**(3), 505–512 (2001)
25. Y. Hu, X. Hu, L. Yan et al., Shim coil set for an open biplanar MRI system using an inverse boundary element method. IEEE Trans. Appl. Supercond. **26**(7), 4403905 (2016)
26. Z. Xu, X. Li, P. Guo et al., Equivalent magnetic dipole method used to design gradient coil for unilateral magnetic resonance imaging. Chin. Phys. B **027**(005), 545–550 (2018)
27. F. Jia, Z. Liu, M. Zaitsev et al., Design multiple-layer gradient coils using least-squares finite element method. Struct. Multidiscip. Optim. **49**(3), 523–535 (2014)
28. G. Shou, X. Ling, L. Feng et al., MRI coil design using boundary-element method with regularization technique: A numerical calculation study. IEEE Trans. Magn. **46**(4), 1052–1059 (2010)
29. H.S. Lopez, F. Liu, M. Poole et al., Equivalent magnetization current method applied to the design of gradient coils for magnetic resonance imaging. IEEE Trans. Magn. **45**(2), 767–775 (2009)
30. D. Calvetti, E. Somersalo, Inverse problems: From regularization to Bayesian inference. Wiley Interdiscip. Rev. Comput. Stat. **10**(3), e1427 (2018)
31. D. Krawczyk-Stando, M. Rudnicki, Regularization parameter selection in discrete ill-posed problems—The use of U-curve. Int. J. Appl. Math. Comput. Sci. **17**, 157–164 (2007)
32. A.N. Tikhonov, Solution of incorrectly formulated problem and the regularization method. Soviet Math. Dokl. **4**, 1035–1038 (1963)
33. A.N. Tikhonov, Regularization of incorrectly posed problems. Soviet Math. Dokl. **4**, 1624–1627 (1963)
34. Y. Wang, Q. Wang, H. Qu et al., Highly shielded gradient coil design for a superconducting planar MRI system. IEEE Trans. Biomed. Eng. **67**(8), 2328–2336 (2020)
35. W. Liu, Zu. Donglin, X. Tang, H. Guo, An optimized target-field method for MRI transverse biplanar gradient coil design. Meas. Sci. Technol. **22**(12), 1863–1868 (2011)

Authors and Affiliations

Sheng Shen[1] · Neha Koonjoo[2] · Xiaohan Kong[1] · Matthew S. Rosen[2,3,4] · Zheng Xu[1]

Sheng Shen
shensheng@cqu.edu.cn

Matthew S. Rosen
msrosen@mgh.harvard.edu

1 State Key Laboratory of Power Transmission Equipment and System Security and New Technology, Chongqing University, Chongqing 400044, China

2 MGH/A.A. Martinos Center for Biomedical Imaging, Charlestown MA, 02129, USA

3 Department of Physics, Harvard University, Cambridge MA, 02138, USA

4 Harvard Medical School, Boston MA, 02115 , USA